

Anisotropy-governed competition of magnetic phases in the honeycomb quantum magnet $\text{Na}_3\text{Ni}_2\text{SbO}_6$ studied by dilatometry and high-frequency ESR

J. Werner,¹ W. Hergert,¹ M. Gertig,¹ J. Park,¹ C. Koo,¹ and R. Klingeler^{1,2,*}

¹*Kirchhoff Institute of Physics, Heidelberg University, INF 227, D-69120 Heidelberg, Germany*

²*Centre for Advanced Materials (CAM), Heidelberg University, INF 225, D-69120 Heidelberg, Germany*

(Received 28 December 2016; revised manuscript received 26 April 2017; published 20 June 2017)

Thermodynamic properties and low-energy magnon excitations of $S = 1$ honeycomb-layered $\text{Na}_3\text{Ni}_2\text{SbO}_6$ have been investigated by high-resolution dilatometry, static magnetization, and high-frequency electron spin resonance studies in magnetic fields up to 16 T. At $T_N = 16.5$ K, there is a tricritical point separating two distinct antiferromagnetic phases, AF1 and AF2, from the paramagnetic regime. In addition, our data imply short-range antiferromagnetic correlations at least up to $\sim 5T_N$. Well below T_N , the magnetic field $B_{C1} \approx 9.5$ T is needed to stabilize AF2 against AF1. The thermal expansion and magnetostriction anomalies at T_N and B_{C1} imply significant magnetoelastic coupling, both of which are associated with a sign change of $\partial L/\partial B$. The transition at B_{C1} is associated with softening of the antiferromagnetic resonance modes observed in the electron-spin-resonance spectra. The anisotropy gap $\Delta = 360$ GHz implies considerable uniaxial anisotropy. We deduce the crucial role of axial anisotropy favoring the AF1 spin structure over the AF2 one. While the magnetostriction data disprove a simple spin-flop scenario at B_{C1} , the nature of a second transition at $B_{C2} \approx 13$ T remains unclear. Both the sign of the magnetostriction and Grüneisen analysis suggest that the short-range correlations at high temperatures are of AF2 type.

DOI: [10.1103/PhysRevB.95.214414](https://doi.org/10.1103/PhysRevB.95.214414)

I. INTRODUCTION

Mott insulators on layered quasi-two-dimensional honeycomb lattices have been found to give rise to a variety of quantum ground states with unusual magnetic excitations. In the $J_1 - J_2 - J_3$ model the nature of the ground states may be of Néel, zigzag, stripe, or spiral type, and it is governed by the first-, second-, and third-nearest-neighbor couplings J_1 , J_2 , and J_3 [1–3]. In the $S = 1/2$ case, the quasiclassical ground states are accompanied by a quantum paramagnetic phase with a valence-bond crystal-type order where a gapped state is found in the vicinity of the quantum critical points [2,4]. Evaluating the $J_1 - J_2$ model using a modified spin-wave method implies a rich phase diagram, too, including gapped and gapless quantum spin liquid phases [5]. The recent finding of nondegenerate band-touching points of the magnon bands and Dirac-like behavior at low energies in theoretical investigations of Heisenberg magnets on a honeycomb lattice in [6] underlines the need for experimental studies of the low-energy collective spin excitations. However, only a few honeycomb systems have been studied using high-frequency electron spin resonance (HF-ESR). In the frustrated $S = 1/2$ honeycomb antiferromagnet $\text{InCu}_{2/3}\text{V}_{1/3}\text{O}_3$, HF-ESR has elucidated the peculiar antiferromagnetic ground state [7,8]. HF-ESR studies on the $S = 3/2$ Heisenberg honeycomb magnet $\text{Bi}_3\text{Mn}_4\text{O}_{12}(\text{NO}_3)$ suggest that geometric frustration is crucial for suppressing long-range antiferromagnetic order [9]. While in the spin-1/2 case the particular spiral ground state is selected by quantum fluctuations, the spin-3/2 system associated with less pronounced quantum fluctuations is found to yield robust nematic order [10].

The $S = 1$ case realized in $\text{Na}_3\text{Ni}_2\text{SbO}_6$ provides further insight into this class of materials as it is a system with small but

even spin number. $\text{Na}_3\text{Ni}_2\text{SbO}_6$ provides a $S = 1$ honeycomb lattice whose interlayer coupling is reasonably small, i.e., about 20 times smaller than the leading intraplane exchange [11]. We observe a tricritical point in zero magnetic field separating the paramagnetic phase from two antiferromagnetic ones, AF1 and AF2, of similar energy. Magnetic fields $B > B_{C1}$ favor the high-field phase AF2 over the ground state AF1. The $q = 0$ low-energy magnon excitations studied by means of antiferromagnetic resonance (AFMR) imply an anisotropy gap $\Delta = 360$ GHz. At $T = 4.2$ K, in addition to the field-induced phase transition at $B_{C1} \approx 9.5$ T there is a second one at $B_{C2} \approx 13$ T. Both transitions affect the dynamic response of the AFMR modes. The magnetostriction data disprove a simple spin-flop scenario at B_{C1} but support the picture of anisotropy-governed competition of antiferromagnetic phases. Interestingly, both the sign of the magnetostriction $\partial L/\partial B$ and the Grüneisen scaling suggest that short-range antiferromagnetic correlations present at least up to $\sim 5T_N$ are of AF2 type. We deduce the crucial role of the axial anisotropy favoring the AF1 spin structure over the AF2 one.

II. EXPERIMENT

Polycrystalline $\text{Na}_3\text{Ni}_2\text{SbO}_6$ was prepared by conventional solid-state synthesis as reported in Ref. [11]. Static magnetization was studied in magnetic fields up to 15 T by means of a home-built vibrating sample magnetometer (VSM) and in fields up to 5 T in a Quantum Design MPMS-XL5 superconducting quantum interference device (SQUID) magnetometer [12]. The relative length changes dL/L were studied on a cuboidal-shaped pressed pellet whose dimension in the measurement direction is 3.28 mm. The measurements were done by means of a three-terminal high-resolution capacitance dilatometer [13]. In order to investigate the effect of magnetic fields, the thermal expansion coefficient

*klingeler@kip.uni-hd.de

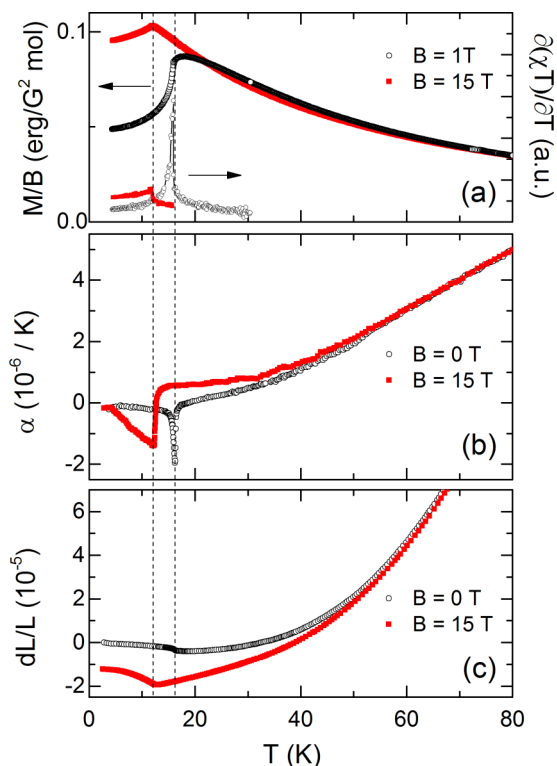


FIG. 1. (a) Static magnetization $\chi = M/B$ and magnetic specific heat $\partial(\chi T)/\partial T$, (b) thermal expansion coefficient, and (c) relative length changes of $\text{Na}_3\text{Ni}_2\text{SbO}_6$ vs temperature at $B = 0$ and 15 T. Vertical dashed lines show T_N in the respective field.

$\alpha = (1/L)[dL(T)/dT]$ was studied in magnetic fields up to 15 T. In addition, the field-induced length changes $dL(B)/L$ were measured at various fixed temperatures in magnetic fields up to 15 T, and the magnetostriction coefficient $\lambda = (1/L)[dL(B)/dB]$ was derived. HF-ESR measurements were carried out using a phase-sensitive millimeter-wave vector network analyzer (MVNA) from AB Millimetrix covering the frequency range from 30 to 1000 GHz and in magnetic fields up to 16 T [14]. For the experiments, a pressed sample pellet of 1.5 mm thickness with a diameter of 4 mm was placed in the sample space of the cylindrical waveguide.

III. RESULTS

Both the thermal expansion coefficient α (at $B = 0$ T) and the magnetic specific heat $\tilde{c}_{p,\text{mag}} \propto \partial(\chi T)/\partial T$ (at $B = 1$ T) derived from the static magnetic susceptibility $\chi = M/B$ show a λ -shaped anomaly, signaling the onset of long-range antiferromagnetic order at $T_N = 16.5 \pm 0.5$ K (Fig. 1). The λ -like anomaly in α is superimposed with a small jump $\Delta\alpha$. Corresponding to the anomalies in α and $\tilde{c}_{p,\text{mag}}$, there is a sharp downturn of the static magnetic susceptibility $\chi = M/B$ and a jumplike increase of the length changes $\Delta L/L \approx 2.2 \times 10^{-6}$ at T_N . The sign of the anomalies in α and dL/L implies a negative hydrostatic pressure effect on the long-range antiferromagnetic order, i.e., $dT_N/dp < 0$.

Application of external magnetic fields suppresses the long-range antiferromagnetically ordered state, as illustrated

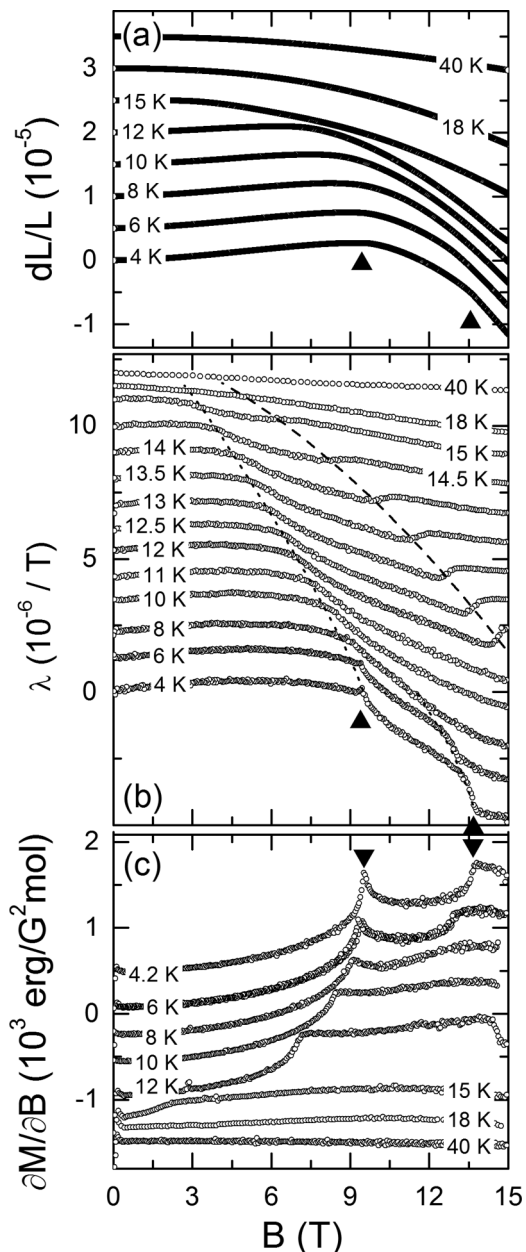


FIG. 2. (a) Relative length changes, (b) magnetostriction coefficient λ , and (c) magnetic susceptibility $\chi = \partial M/\partial B$ of $\text{Na}_3\text{Ni}_2\text{SbO}_6$ vs external magnetic field at constant temperatures from $T = 4$ K to $T = 40$ K. The triangles show the two phase transitions at B_{C1} and B_{C2} at $T = 4$ K. The dashed line indicates B_C ; the dotted lines show the T dependence of B_{C1} and B_{C2} .

by the shift of the anomalies in α and $\tilde{c}_{p,\text{mag}}$ at $B = 15$ T in Fig. 1. In addition to the shift of T_N , the λ -like nature of the anomalies changes to a rather jumplike feature. Note that the length changes dL/L at $B = 15$ T shown in Fig. 1 have been shifted with respect to the zero-field data according to the measured magnetostriction at $T = 30$ K (see Fig. 2). The data at $B = 15$ T imply negative magnetostriction at high magnetic fields in the long-range antiferromagnetically ordered phase as well as in a large temperature regime up to about 80 K, which is about 5 times T_N . As will be discussed below, at temperatures

$T < T_N$, the behavior at magnetic fields $B \lesssim 10$ T is different. In the derivative of magnetization $\partial M/\partial B$ (see Fig. 2), there is a clear increase associated with application of $B = 15$ T at and below T_N , i.e., a left bending of the magnetization curve M vs B . In addition, there is a subtle effect above T_N , too, as at ~ 22 K $\lesssim T \lesssim 60$ K we observe $\chi(15 \text{ T}) < \chi(1 \text{ T})$. In this temperature regime, our data hence imply both negative and relatively large magnetostriction and a slight right curvature of the M vs B curves.

The effect of external magnetic fields is elucidated in more detail in Fig. 2, where the relative magnetostriction $dL(B)/L$, the magnetostriction coefficient $\lambda = (1/L)[dL(B)/dB]$, and the magnetic susceptibility $\partial M(B)/\partial B$ are shown at various constant temperatures. At $T = 4.2$ K, the data show three different phases: At $B < B_{C1} \approx 9.5$ T (phase AF1), there is a positive magnetostriction, signaling expansion of the sample. B_{C1} is associated with a maximum in dL/L , a tiny peak in λ , and a more pronounced peak in $\partial M/\partial B$. In contrast, B_{C2} is associated with a jumplike decrease of λ and an associated step in the magnetic susceptibility. Both the intermediate-field phase at $B_{C1} \leq B \leq B_{C2}$ (i.e., AF2) and the high-field phase at $B > B_{C2}$ (i.e., AF3) are characterized by negative magnetostriction with, however, different values of λ .

Upon heating up to ~ 10 K, there is a moderate suppression of B_{C1} and B_{C2} . Correspondingly, the peaks in $\partial M/\partial B$ and λ transform into kinklike features, with the kink at B_{C1} being more pronounced than the one at B_{C2} . The low-temperature slopes at 4.2 K of the phase boundaries amount to $dT_{C1}/dB \approx -9.3$ K/T and $dT_{C2}/dB \approx -5.2$ K/T, respectively. At higher temperature, the slope $B_{C1}(T)$ becomes steeper, and the data indicate a strong suppression of B_{C1} . In addition, at $T \geq 12$ K, there is a step in the magnetostriction coefficient at B_C associated with the antiferromagnetic phase boundary $T_N(B)$. The well-separated phase boundaries B_C and B_{C1} are particularly evident if the magnetostriction data at $13 \text{ K} \leq T \leq 15 \text{ K}$ are considered because they exhibit a broad maximum and a step downwards at lower field (signaling B_{C1}) followed by a step upwards at somehow higher fields (signaling B_C).

The magnetic field effect on both $\chi(T)$ and $\tilde{c}_{p,\text{mag}} \propto \partial(\chi T)/\partial T$ in the vicinity of $T_N(B)$ is shown in Fig. 3. Upon application of $B \geq 1$ T, the anomaly in $\tilde{c}_{p,\text{mag}}$ significantly broadens and covers a regime of, depending on B , 2 to 4 K. At high fields, only the high-temperature edge of the anomaly is observed as a step. While this step on the right side of the anomalies signals $T_N(B)$, a comparison with the magnetostriction data suggests that the low-temperature kinks of the broad anomalies at $5 \text{ T} \lesssim B \lesssim 8 \text{ T}$ are associated with the phase boundary $B_{C1}(T)$. A similar behavior is observed in the thermal expansion coefficient α (Fig. 4). The anomaly gradually changes from a λ -type shape to a step-type one (see also Fig. 1) while the left shoulder widens. Correspondingly, there is an increasing temperature regime with anomalous length changes which, e.g., at $B = 8$ T extends between 15 and 11 K. As will be seen in the magnetic phase diagram, the anomalous length changes signal the AF2 phase appearing between $T_N(8 \text{ T}) = 15$ K and $T_{C1}(8 \text{ T}) = 11$ K.

Summarizing the thermodynamic data yields the phase diagram in Fig. 5. At zero magnetic field, the long-range antiferromagnetically ordered phase AF1 below T_N is associated

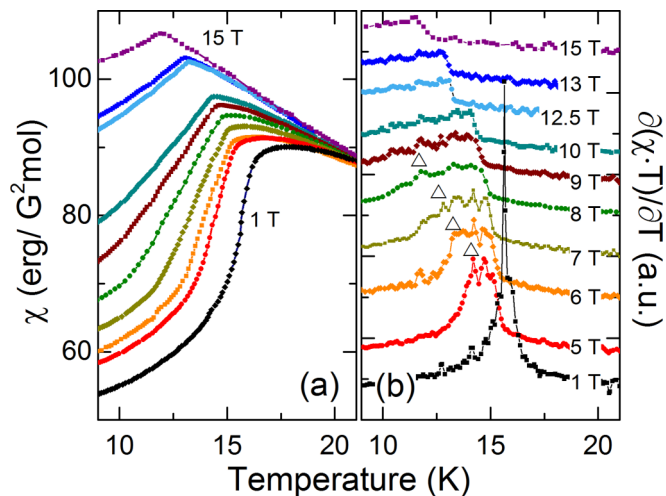


FIG. 3. Evolution of (a) static magnetic susceptibility and (b) the associated magnetic specific heat $\partial(\chi T)/\partial T$ vs temperature upon application of various constant magnetic fields. Open triangles show $T_{C1}(B)$ [i.e., $B_{C1}(T)$].

with positive magnetostriction. In addition, there is a large regime up to about 80 K where external magnetic fields cause shrinking of the sample volume. As will be corroborated by the HF-ESR data shown below, this regime is characterized by short-range antiferromagnetic order. According to $\partial L/\partial B = -\partial M/\partial p$, positive magnetostriction signals a magnetization decrease upon application of hydrostatic pressure and vice versa. Hence, our data show that, below T_N , application of hydrostatic pressure will be associated with decreasing magnetization, and the opposite behavior is realized for $T > T_N$. This observation implies that the short-range correlations are

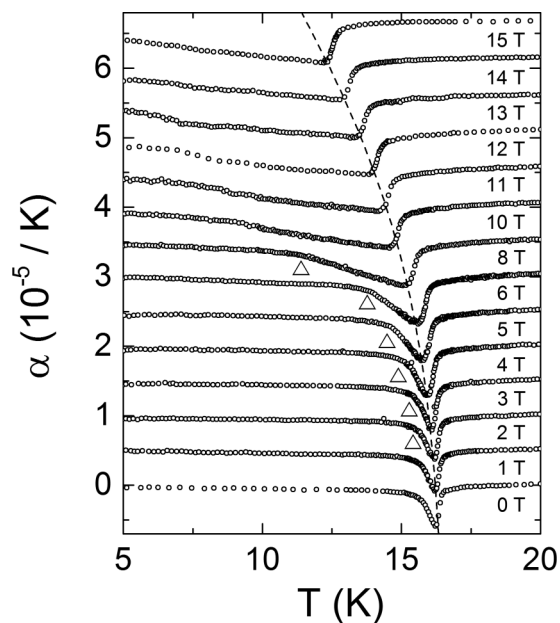


FIG. 4. Thermal expansion coefficient at various constant magnetic fields (data are shifted). The dashed line indicates $T_N(B)$, and the open triangles show $T_{C1}(B)$ [i.e., $B_{C1}(T)$].

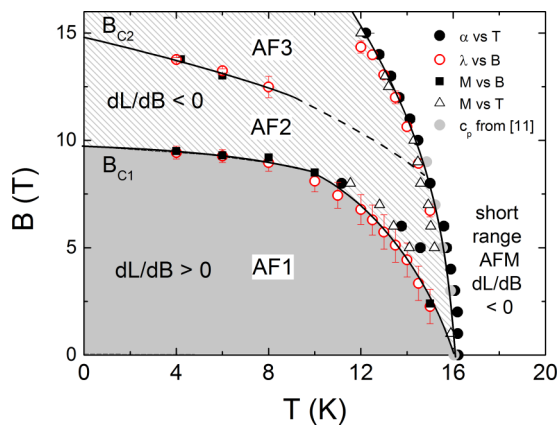


FIG. 5. Magnetic phase diagram of polycrystalline $\text{Na}_3\text{Ni}_2\text{SbO}_6$ as constructed from thermal expansion, magnetostriction, and magnetization data. AF1 labels long-range antiferromagnetic order with positive magnetostriction $\lambda > 0$; AF2 and AF3 indicate antiferromagnetically ordered phases with $\lambda < 0$.

not of AF1 type. In addition, the data show a tricritical point at T_N which separates a competing long-range ordered AF2 phase with $\lambda < 0$ from the $\lambda > 0$ long-range ordered AF1 and the $\lambda < 0$ short-range AF ordered phases. At finite magnetic fields $B < B_{C2}$, this phase appears in between AF1 and the short-range ordered one. Finally, at $B > B_{C2}$, there is a third antiferromagnetic phase (AF3), again with $\lambda < 0$, whose phase boundary is associated with a jump in λ .

As seen in the magnetic susceptibility $\partial M/\partial B$ as well as in the magnetostriction coefficient, both anomalies are sharp, and their nature is different, i.e., rather peaklike at B_{C1} and jumplike at B_{C2} . This excludes a common origin of the anomalies where B_{C1} and B_{C2} would reflect different relative orientations of the individual crystallites with respect to the external magnetic field. In addition, even when assuming the largest g factor anisotropy consistent with our data, this effect is much too small to account for the large differences between B_{C1} and B_{C2} .

Additional information about the nature of the spin-ordered phases is obtained by comparing the anomalous, i.e., magnetic, contributions to the thermal expansion coefficient and to the specific heat, α^{magn} and $c_{p,\text{mag}}$, respectively. Using the Grüneisen relation

$$\Gamma = \frac{\alpha^{\text{magn}}}{c_{p,\text{mag}}} = \frac{1}{V} \frac{\partial \ln \epsilon}{\partial p} \Big|_T \quad (1)$$

enables determination of the hydrostatic pressure dependence of the associated, i.e., magnetic, energy scales ϵ . The magnetic specific heat $c_{p,\text{mag}}$ has been taken from Ref. [11]. The phonon contribution to the thermal expansion coefficient is accounted for by scaling the specific heat of the nonmagnetic counterpart $\text{Li}_3\text{Zn}_2\text{SbO}_6$, which was used in Ref. [11] to obtain the magnetic specific heat. As expected, for the phonon contributions to α and c_p obtained with this procedure we find a single Grüneisen relation in the whole temperature range under study. The resulting volumetric phonon Grüneisen parameter amounts to $\Gamma_{\text{phon}} = 1.9(1) \times 10^{-7}$ mol/J. The anomalous contributions to α and c_p , viz., the anomalous

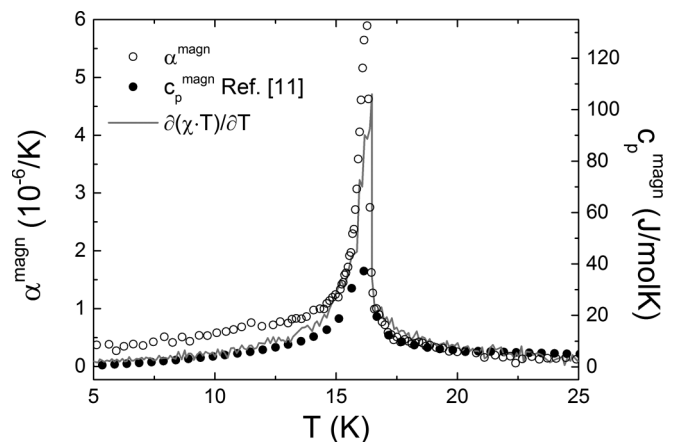


FIG. 6. Magnetic contribution to the thermal expansion α^{magn} and to the specific heat $c_{p,\text{mag}}$ (from Ref. [11]) as well as the magnetic specific heat $\tilde{c}_{p,\text{mag}} \propto \partial(\chi T)/\partial T$.

magnetic length and entropy changes, are shown in Fig. 6. For comparison, we also add the magnetic specific heat $\partial(\chi T)/\partial T$ derived from the static susceptibility. The data show that the anomalies in the thermal expansion coefficient and in the specific heat can be scaled to each other at $T > T_N$ by applying the Grüneisen parameter $\Gamma_{\text{afm}} = -4.6(2) \times 10^{-8}$ mol/J. With $V_{u.c.} = 108.35 \text{ \AA}^3$ [15], our analysis yields $\partial \ln \epsilon/\partial p = -3.0(2) \times 10^{-3}/\text{GPa}$. Assuming ϵ is proportional to T_N , this corresponds to a small hydrostatic pressure dependence $dT_N/dp = -0.049(3) \text{ K/GPa}$. For $T < T_N$, α^{magn} and $c_{p,\text{mag}}$ do not scale but show the same temperature dependence. To be specific, the same Grüneisen parameter Γ_{afm} as the one found for $T \geq T_N$ can be used if the step $\Delta\alpha^{\text{magn}} = -3.7 \times 10^{-7}/\text{K}$ is considered.

IV. HIGH-FREQUENCY ELECTRON SPIN RESONANCE

ESR spectra taken at $f = 388 \text{ GHz}$ [Fig. 7(b)] and at 280 GHz (not shown) show a broad ($\sim 1 \text{ T}$) resonance line

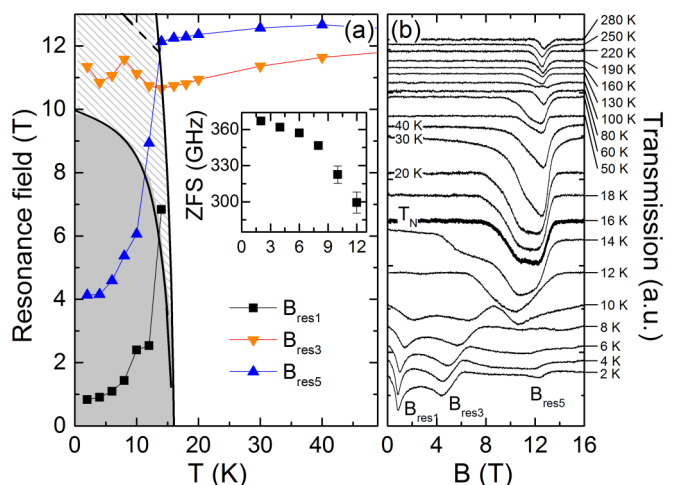


FIG. 7. (a) Resonance fields at 388 GHz vs temperatures between 2 and 50 K and (b) corresponding HF-ESR spectra in the temperature range 2–280 K. The thick line is the spectrum at $T_N(B = 0)$. Inset: Zero-field splitting (ZFS) vs temperature.

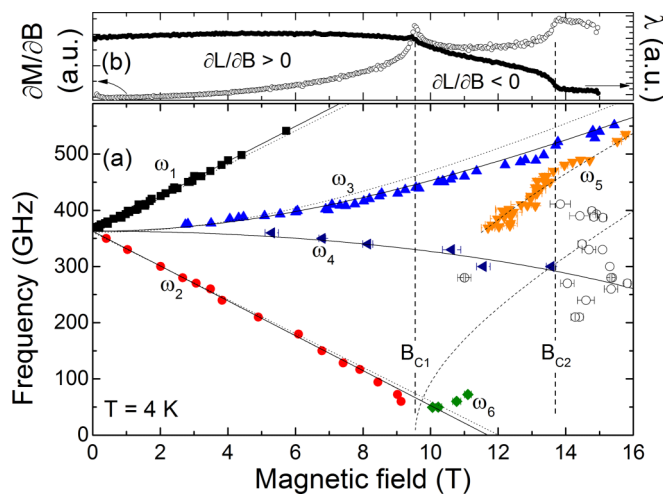


FIG. 8. (a) HF-ESR absorption frequencies vs magnetic field at $T = 4$ K. Solid (dotted) lines represent fits with anisotropic (isotropic) g factor according to Eqs. (2) to (4). (b) Magnetic susceptibility $\partial M/\partial B$ and magnetostriction coefficient λ at $T = 4$ K vs external magnetic field. Vertical dashed lines show the critical fields B_{C1} and B_{C2} .

at $T > 160$ K. At high temperature, the resonance field at both frequencies corresponds to the effective g factor of $g = 2.17 \pm 0.03$. Both the observation of a single rather isotropic line and the value of the g factor agree with low-field ESR data at high temperatures where $g = 2.15$. This value from X-band ESR still slightly increases upon heating at 300 K [11]. Upon cooling, the resonance feature shifts and asymmetrically broadens at $T \leq 80$ K. As seen in Fig. 7(a), below T_N in addition to the broadening there is a splitting and considerable shift of the resonance lines which is typically observed in AFMR spectra due to the evolution of internal fields. In the long-range spin-ordered state where HF-ESR is susceptible to collective $q = 0$ spin excitations, three AFMR features are observed at $f = 388$ GHz and at 280 GHz [see Fig. 7(b)]. With decreasing temperature, the antiferromagnetic resonance lines shift to lower fields for $f = 388$ GHz and to higher fields for $f = 280$ GHz.

HF-ESR measurements at various fixed frequencies enable constructing the magnetic resonance field vs frequency phase diagram at $T = 4$ K, as shown in Fig. 8(a). The vertical dashed lines correspond to B_{C1} and B_{C2} from the magnetostriction and magnetization measurements [see Fig. 8(b)]. In the AF1 phase, four clearly separated resonance branches ω_1 to ω_4 are observed. At low fields, all branches merge into a common feature associated with a zero-field gap of $\Delta = 360$ GHz. Upon crossing the phase boundary $B_{C1}(4 \text{ K}) = 9.5$ T, two of the branches, i.e., $\omega_{3,4}$, remain rather unaffected, while the branches $\omega_{1,2}$ are not observed in AF2. In contrast, a new resonance branch, ω_5 , is observed in AF2. Neither this new branch ω_5 nor ω_3 shows changes at B_{C2} , i.e., when approaching AF3.

The four branches in AF1 suggest a two-sublattice AFMR model with an axial-type anisotropy. Quantitatively, the resonance branches in the uniaxial two-sublattice model are

described by the equations [16]

$$\omega_3 = \sqrt{\Delta^2 + (\gamma_{\perp} B)^2}, \quad (2)$$

$$\omega_4 = \sqrt{\Delta^2 (1 - B^2/B_E^2)} \quad (3)$$

for the case when the anisotropy field B_A and the external magnetic field B are orthogonal. $\Delta = \gamma \sqrt{2B_E B_A + B_A^2}$ is the zero-field splitting, B_E is the exchange field, and $\gamma_i = g_i \mu_B$ is the gyromagnetic ratio. The case of B parallel to B_A and below B_{SF} is associated with the AFMR modes [16]

$$\omega_{1,2} = \Delta \pm \gamma_{\parallel} B. \quad (4)$$

For further analysis, we estimate $B_E \approx 23$ T from the saturation field of the magnetization [11]. Fitting the resonance modes by using an isotropic g factor describes the data reasonably well up to about $B \sim 6$ T (see the dotted lines in Fig. 8). Quantitatively, we retrieve $B_A = (2.9 \pm 0.5)$ T and $g = 2.15 \pm 0.03$. Note, however, that in addition to discrepancies around B_{C1} and in the phases AF2 and AF3 which will be discussed below, application of an anisotropic g factor resembles the experimental data significantly better (see the solid lines in Fig. 8). To be specific, there is a slightly improved description of the $\omega_{1,2}$ modes in AF1, and ω_3 is much better described in the whole field range. In this case, we obtain $B_A = (2.9 \pm 0.5)$ T, $g_{\parallel} = 2.22 \pm 0.01$, and $g_{\perp} = 1.98 \pm 0.02$. In both cases, rather large values of the anisotropy field in comparison to the exchange field are obtained, which underlines the importance of considering the higher-order terms in Eqs. (2) to (4).

In the frame of the uniaxial AFMR model applied here, at $T = 4$ K a spin-flop transition is expected at $B_{SF} = (11.7 \pm 0.5)$ T which is slightly larger than $B_{C1} = (9.5 \pm 0.1)$ T. We recall that, at B_{C1} , there are structural changes and a sign change of the magnetostriction coefficient which excludes a simple spin-flop nature of the B_{C1} transition. This conclusion is supported by the fact that the spin-flop mode expected in the two-sublattice model with uniaxial anisotropy at $B > B_{SF}$ is not observed. Neither the parameters obtained in the AF1 phase [$B_{SF} = (11.7 \pm 0.5)$ T] nor the two-sublattice model employing the (hypothetical) spin-flop field of B_{C1} [see the dashed line in Fig. 8(a)] or any smaller but finite spin-flop field describe the AFMR mode ω_5 . As B_{C1} is associated with changes in the lattice we can exclude neither changes in the spin structure at B_{C1} nor changes in the anisotropy towards a more complex anisotropy as would be present in an orthorhombic symmetry with several anisotropy axes. Based on the observed mode ω_5 , however, and without information on the actual spin structure realized in the high-field phases, no clear conclusions about the details of the anisotropy at high fields can be drawn. In the phase AF3 we observe several resonance features in addition to the resonance branches ω_3 and ω_5 in the frequency range 200 to 420 GHz which do not form a resonance branch [open circles in Fig. 8(a)].

Finally, we analyze the temperature dependence of the resonance fields as seen in Fig. 7. The three resonance features showing up in the spectra at 388 GHz refer to the resonance branches ω_1 , ω_3 , and ω_5 . The shift in the resonances upon cooling directly measures the evolution of the internal magnetic field, i.e., the internal exchange-anisotropy

field strength $B_{EA} = \sqrt{2B_E B_A + B_A^2}$. In the framework of the two-sublattice model, the data hence allow extracting the antiferromagnetic order parameter $B_{EA} \propto \langle S \rangle$ or the zero-field splitting $\Delta = \gamma B_{EA}$. The resulting temperature dependence $\Delta(T)$ of this order parameter is shown in the inset of Fig. 7(a).

V. DISCUSSION

The phase diagram of $\text{Na}_3\text{Ni}_2\text{SbO}_6$ shows a tricritical point at T_N . It separates two different long-range antiferromagnetically ordered phases from the paramagnetic one. The latter exhibits short-range antiferromagnetic order up to at least 80 K, as evidenced by the thermal expansion coefficient and the evolution of the ESR resonance feature. It is further supported by the observation of rather large anomalous magnetostriction in this temperature range. This direct experimental evidence for short-range correlations extending up to more than $5T_N$ agrees with the fact that, below 25 K, only about 60% of the total magnetic entropy is released [11]. The field dependence of the length changes is negative both in AF2 and in the paramagnetic phase, while it is positive in AF2. This implies opposite hydrostatic pressure effects; that is, short-range correlations above T_N are not of AF1 type. This conclusion is supported by the Grüneisen analysis. Since both AF2 and the paramagnetic, i.e., short-range ordered, phase share the same sign for the pressure dependence, we suppose the short-range correlations are of AF2 type.

The phase boundary $B_{C1}(T)$ [or $T_{C1}(B)$] separating AF1 and AF2 is, at low temperatures, presumably of weak first order character, as indicated by a tiny jump in the magnetization $\Delta M_{C1} \approx 0.12\mu_B/\text{f.u.}$ Analyzing the associated entropy changes by means of the Clausius-Clapeyron relation $dB_{C1}/dT = -\Delta S_{C1}/\Delta M_{C1}$ yields only small entropy changes of $\Delta S_{C1} \approx 75 \text{ mJ}/(\text{mol K})$ associated with B_{C1} , i.e., with changing from AF1 to AF2 (see the phase diagram in Fig. 5). Indeed, we expect only small entropy differences in the spin configurations AF1 and AF2 as both phases develop long-range order at the same T_N . This finding somehow agrees with the observation that the Grüneisen relation is very similar above and below T_N except for a jump in the thermal expansion coefficient α . As described above, the short-range antiferromagnetic order may be of AF2 type with a volume slightly different from the AF1-type phase, as shown by the thermal expansion and magnetostriction anomalies. On the other hand, the entropies of the spin configurations AF1 and AF2 are very similar.

Magnetic anisotropy in $\text{Na}_3\text{Ni}_2\text{SbO}_6$ is of uniaxial nature, which is typical for Ni^{2+} systems with octahedral coordination of the metal ions. Below B_{C1} , the AFMR modes are well described by means of a two-sublattice model which agrees with the stripelike spin configuration derived from previous density-functional-theory studies [11]. However, possible competing phases in the $J_1 - J_2 - J_3$ honeycomb-lattice model such as the Néel and zigzag-type phases are not excluded either by our data. In contrast, spiral-type antiferromagnetic phases are not compatible with the two-sublattice description. The high-field phase AF2, however, cannot be described in this two-sublattice scenario as the branches ω_5 and ω_6 are not explained. Intriguingly, the branches ω_5 and ω_6 suggest a change in the behavior at around 11.7 T, where no thermodynamic signature of a

phase transition is visible. In order to further elucidate these discrepancies, experimental studies of the spin structure in phases AF2 and AF3 and/or HF-ESR studies on single crystals are desirable. For example, in the triangular spin-1/2 system $\text{Lu}_2\text{Cu}_2\text{O}_5$ the AFMR modes are well described in terms of a six-sublattice model where the modes associated with $B \perp B_A$ are not affected by metamagnetic transitions, yielding a high-field state with a cone spin structure [17]. Without additional knowledge of the spin structure or observation of further branches, however, no reliable model can be constructed for the high-field phases.

The HF-ESR data and X-band ESR data indicate an isotropic g factor at high temperatures, which is typical for Ni^{2+} ions in a slightly distorted octahedral environment [18]. Since the field-induced transitions at B_{C1} and B_{C2} imply changes in the atomic and spin structures, the observed deviations of the low-field model from the experimental data may be attributed to these transitions. Due to the fact that there are considerable deviations already well below B_{C1} , our data do not exclude anisotropy of g at low temperatures. The resulting values of the anisotropic g factors would be, however, very unusual for Ni^{2+} ions. Instead, large anisotropy $g_{\perp} = 2.314$ and $g_{\parallel} = 1.967$ have been measured in NaNiO_2 , in which it is attributed to the cooperative Jahn-Teller effect of the Ni^{3+} ions [19]. However, the rather small thermal expansion renders a very strongly distorted local environment of the Ni^{2+} ions in AF1 unlikely.

The phase boundary $B_{C1}(T)$ appears at a slightly lower field than expected for the spin-flop transition in the uniaxial two-sublattice model. As the AF1 to AF2 transition is associated with lattice changes, the transition has a weak first-order character. The observed magnetostrictive effect at B_{C1} , the changes in the AFMR modes at B_{C1} , and, particularly, the changes in the sign of the magnetostriction coefficient λ exclude a simple spin-flop nature of the transition between AF1 and AF2. Instead, AF2 appears to be stabilized when the external magnetic field nearly overcomes uniaxial anisotropy by means of spin reorientation. We hence conclude that spin configuration AF2 is disfavored with respect to AF1 at small magnetic fields by magnetic anisotropy. First, this is suggested by the sign of the magnetostriction coefficient, which excludes the short-range antiferromagnetic fluctuation being of AF1 type and rather suggests AF2 type. However, while at T_N a tricritical point suggests similar energies for AF1 and AF2, well below T_N the AF2 phase is stabilized only in magnetic fields which are comparable to but slightly below the spin-flop field. Our results hence imply that anisotropy is crucial for stabilization of the actual antiferromagnetic ground state, i.e., AF1.

VI. SUMMARY

The phase diagram of $S = 1$ honeycomb-layered $\text{Na}_3\text{Ni}_2\text{SbO}_6$ exhibits two competing antiferromagnetic phases which display a tricritical point at T_N . The low-energy magnon excitations studied well below T_N suggest a magnetic two-sublattice phase AF1 with considerable uniaxial anisotropy showing up in the anisotropy gap of $\Delta = 360 \text{ GHz}$. Application of external magnetic fields stabilizes AF2 at B_{C1} , which is smaller than the anisotropy-exchange field but has

similar order. A simple spin-flop scenario is excluded by the magnetostriction data as well as by the absence of the spin-flop resonance mode. In the paramagnetic phase, both the thermodynamic and local probe studies show antiferromagnetic fluctuations up to at least $5T_N$. However, short-range order is not of AF1 type. We hence conclude a subtle interplay of AF1- and AF2-type spin orders which is driven to the actual low-temperature AF1 ground state by magnetic anisotropy.

ACKNOWLEDGMENTS

The authors thank E. Zvereva and A. U. B. Wolter for valuable support and V. B. Nalbandyan for providing the sample for this study. We thank R. Valenti, V. Kataev, and A. Tsirlin for fruitful discussions. J.W. acknowledges support from the IMPRS-QD and by the Excellence Initiative of the German Federal Government.

-
- [1] J. Fouet, P. Sindzingre, and C. Lhuillier, *Eur. Phys. J. B* **20**, 241 (2001).
- [2] P. H. Y. Li, R. F. Bishop, D. J. J. Farnell, and C. E. Campbell, *Phys. Rev. B* **86**, 144404 (2012).
- [3] D. C. Cabra, C. A. Lamas, and H. D. Rosales, *Phys. Rev. B* **83**, 094506 (2011).
- [4] R. F. Bishop, P. H. Y. Li, O. Götze, J. Richter, and C. E. Campbell, *Phys. Rev. B* **92**, 224434 (2015).
- [5] E. Ghorbani, F. Shahbazi, and H. Mosadeq, *J. Phys. Condens. Matter* **28**, 406001 (2016).
- [6] J. Fransson, A. M. Black-Schaffer, and A. V. Balatsky, *Phys. Rev. B* **94**, 075401 (2016).
- [7] M. Yehia, E. Vavilova, A. Möller, T. Taetz, U. Löw, R. Klingeler, V. Kataev, and B. Büchner, *Phys. Rev. B* **81**, 060414(R) (2010).
- [8] S. Okubo, F. Elmasry, W. Zhang, M. Fujisawa, T. Sakurai, H. Ohta, M. Azuma, O. A. Sumirnova, and N. Kumada, *J. Phys.: Conf. Ser.* **200**, 022042 (2010).
- [9] S. Okubo, H. Wada, H. Ohta, T. Tomita, M. Fujisawa, T. Sakurai, E. Ohmichi, and H. Kikuchi, *J. Phys. Soc. Jpn.* **80**, 023705 (2011).
- [10] A. Mulder, R. Ganesh, L. Capriotti, and A. Paramekanti, *Phys. Rev. B* **81**, 214419 (2010).
- [11] E. A. Zvereva, M. I. Stratan, Y. A. Ovchenkov, V. B. Nalbandyan, J.-Y. Lin, E. L. Vavilova, M. F. Iakovleva, M. Abdel-Hafiez, A. V. Silhanek, X.-J. Chen, A. Stroppa, S. Picozzi, H. O. Jeschke, R. Valenti, and A. N. Vasiliev, *Phys. Rev. B* **92**, 144401 (2015).
- [12] R. Klingeler, B. Büchner, K.-Y. Choi, V. Kataev, U. Ammerahl, A. Revcolevschi, and J. Schnack, *Phys. Rev. B* **73**, 014426 (2006).
- [13] L. Wang, U. Köhler, N. Leps, A. Kondrat, M. Nale, A. Gasparini, A. de Visser, G. Behr, C. Hess, R. Klingeler, and B. Büchner, *Phys. Rev. B* **80**, 094512 (2009).
- [14] P. Comba, M. Großhauser, R. Klingeler, C. Koo, Y. Lan, D. Müller, J. Park, A. Powell, M. J. Riley, and H. Wadepohl, *Inorg. Chem.* **54**, 11247 (2015).
- [15] W. Schmidt, R. Berthelot, A. W. Sleight, and M. A. Subramanian, *J. Solid State Chem.* **201**, 178 (2013).
- [16] G. T. Rado and H. Suhl, *Magnetism*, Vol. 1 (Academic Press, New York, London, 1963).
- [17] T. Goto, S. Kimura, S. Okubo, H. Ohta, and M. Motokawa, *Appl. Magn. Reson.* **18**, 463 (2000).
- [18] J. Krzystek, A. Ozarowski, and J. Telsner, *Coord. Chem. Rev.* **250**, 2308 (2006).
- [19] E. Chappel, M. D. Núñez-Regueiro, F. Dupont, G. Chouteau, C. Darie, and A. Sulpice, *Eur. Phys. J. B* **17**, 609 (2000).